Extremely fast electrochromic supercapacitors based on mesoporous WO₃ prepared by an evaporation-induced self-assembly

Keon-Woo Kim[1], Tae Yong Yun[2], Sang-Hoon You[3], Xiaowu Tang[4], Jaeyong Lee[1], Yeseong Seo[1], Yong-Tae Kim [3], Se Hyun Kim [4], Hong Chul Moon [2] and Jin Kon Kim [1]

Abstract

Mesoporous metal oxides consisting of fully interconnected network structures with small pores (20–50 nm) have high surface areas and decreased ion intercalation distances, making them ideal for use in high-performance electrochromic supercapacitors (ECSs). Evaporation-induced self-assembly (EISA), which combines sol–gel chemistry and molecular self-assembly, is a powerful method for the fabrication of mesoporous metal oxides through a solution phase synthesis. Herein, we introduce ultrafast sub-1 s ECSs based on an amorphous mesoporous tungsten trioxide (WO₃) that is prepared by EISA. Compared to that of a compact-WO₃ film-based device, the performances of an ECS with mesoporous WO₃ exhibits a large optical modulation (76% at 700 nm), ultrafast switching speeds (0.8 s for coloration and 0.4 s for bleaching), and a high areal capacitance (2.57 mF/cm²), even at a high current density (1.0 mA/cm²). In addition, the excellent device stability during the coloration/bleaching and charging/discharging cycles is observed under fast response conditions. Moreover, we fabricated a patterned mesoporous WO₃ for ECS displays (ECSDs) via printing-assisted EISA (PEISA). The resulting ECSDs can be used as portable energy-storage devices, and their electrochromic reflective displays change color according to their stored energy level. The ECSDs in this work have enormous potential for use in next-generation smart windows for buildings and as portable energy storage displays.

Introduction

Electrochromic devices (ECDs), which control light transmittance through electrochemical redox reactions, have been widely used in electrochemical reflective displays or smart windows for energy efficient buildings[1–5]. Recently, the functionality of ECDs has been extended to include energy storage, which is referred to as electrochromic supercapacitors (ECSs)[6–9]. ECSs have been increasingly studied as next-generation electrochemical components that can not only change their own optical properties but also store the energy supplied for coloration. In particular, their optical characteristics, such as color intensity, directly reflect the real-time levels of energy stored in these devices[10–15].

One key parameter for achieving high-performance ECSs is an EC chromophore. Among EC materials, transition metal oxides such as tungsten trioxide (WO₃) have been widely employed to exploit their superior electrochemical properties[16–18], large optical modulation[19,20], and high coloration efficiency[21,22]. Recently, a few research groups reported ECSs based on WO₃ films[23–26]. Mai et al fabricated ECSs with WO₃ films prepared by thermal evaporation. However, the diffusivity of Li⁺ ions across the film was low because a dense WO₃ layer was formed by

Correspondence: S. H.K. (shkim97@yu.ac.kr) or H. C.M. (hcmoon@uos.ac.kr) or J. K.K. (jkkim@postech.ac.kr)
¹National Creative Research Initiative Center for Smart Block Copolymer Self-Assembly, Department of Chemical Engineering, Pohang University of Science and Technology (POSTECH), Pohang, Gyungbuk 790-784, Republic of Korea
²Department of Chemical Engineering, University of Seoul, Seoul 02504, Republic of Korea
Full list of author information is available at the end of the article

the thermal evaporation process[27]. Additionally, the diffusion distance for sufficient intercalation was relatively long from the surface of the WO_3 film, thereby resulting in a slow switching speed and unsatisfactory optical modulation. To overcome these drawbacks arising from the dense WO_3 structure, various WO_3 nanostructures, such as nanosheets, nanoparticles, and macroporous films, have been suggested[28–32]. However, the ultrafast dynamics needed for practical applications, such as displays, cannot be achieved with these nanostructured WO_3 because the interfacial area where ion intercalation occurs is not sufficiently large and the ion diffusion distance is still relatively long. Therefore, mesoporous structures consisting of fully interconnected small pores (diameters of 2–50 nm) are considered an ideal nanostructure for realizing the ultrafast response of devices[33,34].

Hard templating methods have often been used to fabricate mesoporous structures, but a multistep process is necessary, and the range of tunable pore sizes is limited[35–41]. On the other hand, evaporation-induced self-assembly (EISA) based on sol-gel chemistry and the self-assembly of amphiphilic molecules (e.g., block copolymers) is a powerful technique capable of producing various mesoporous metal oxides[42–45]. The pore size of the resulting mesoporous metal oxides is easily controlled by adjusting the volume ratio of hydrophobic and hydrophilic parts in amphiphilic molecules[46,47]. Moreover, this method can be combined with versatile solution processes, such as spray-coating, spin-coating, dip-coating, and printing[48–52].
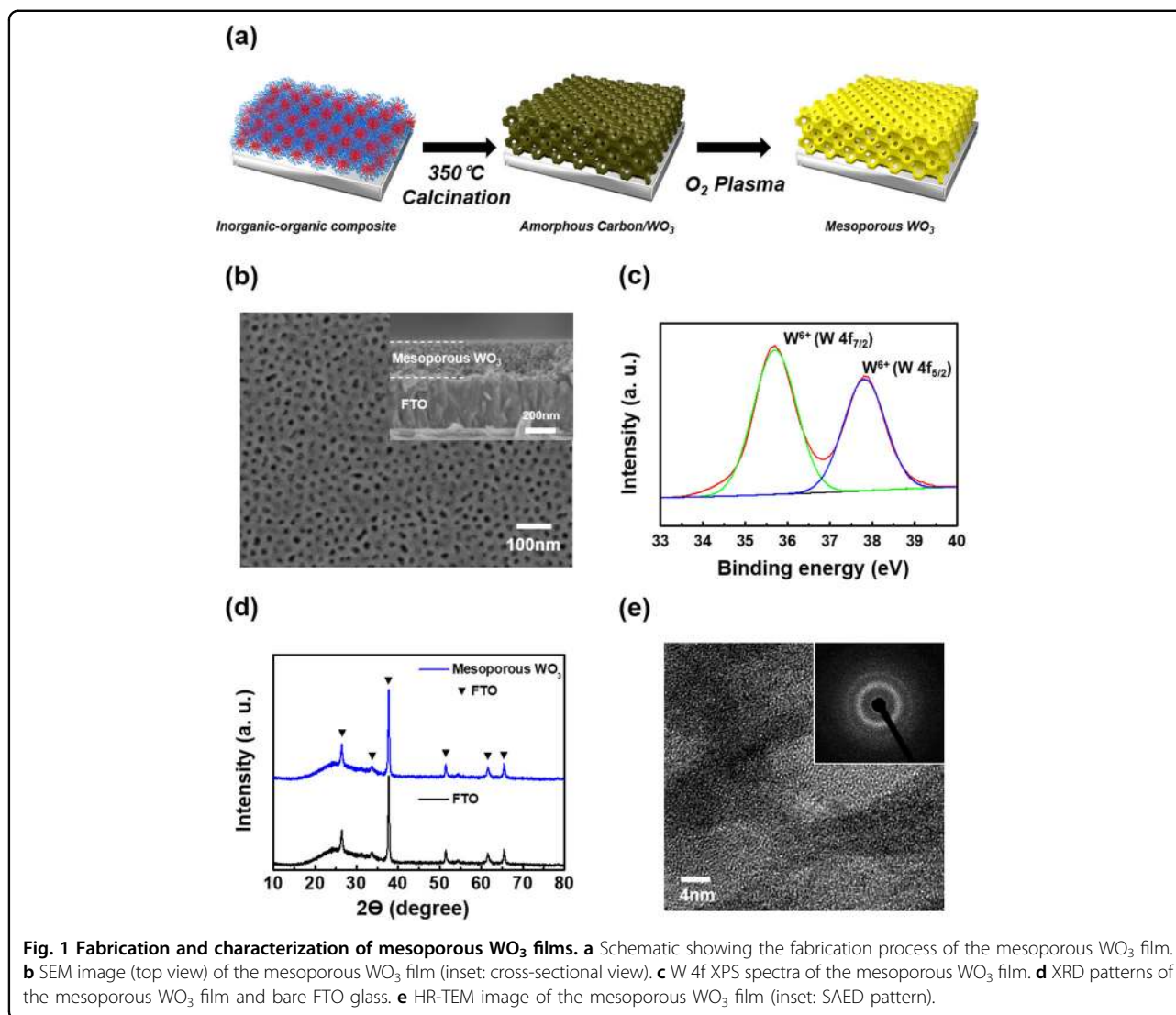
Herein, we report ultrafast response ECSs by exploiting the mesoporous structure of an amorphous WO_3 film prepared by EISA. Compared to compact-WO_3 film-based devices, mesoporous WO_3 devices showed outstanding electrochromic/supercapacitor properties, for example, a large optical modulation ($\Delta T = 76\%$), ultrafast sub-1 s switching speeds ($t_c = 0.8$ s and $t_b = 0.4$ s), and excellent coloration/bleaching and charging/discharging stability under fast switching conditions. By exploiting the ultrafast response, we successfully demonstrated functional ECS displays (ECSDs) showing user-customized images and storing the energy supplied for coloration. To this end, the EISA protocol and printing technology were combined for patterning mesoporous WO_3, which is referred to as printing-assisted EISA (PEISA). The energy stored in the ECSDs can be extracted for the operation of other electronic devices, such as LEDs. These highly functional energy-storing ECSDs have great potential for use in next-generation smart electrochemical components.

Results and discussion

Figure 1a illustrates the fabrication process of a mesoporous WO_3 film through EISA. First, a mixed solution of tetrahydrofuran (THF) including polystyrene-*block*-polyethylene oxide (PS_{19k}-*b*-$PEO_{6.5k}$) and ethanol-containing WCl_6 as a WO_3 precursor was spin-coated on FTO-coated glass. The resulting film was comprised of inorganic-organic composites. The THF evaporated first due to its low boiling point, and then PS_{19k}-*b*-$PEO_{6.5k}$ formed spherical micelles where hydrophobic PS blocks were surrounded by PEO shells containing hydrolyzed hydrophilic inorganic tungsten species[53,54]. The composite was calcined at 350 °C for 1 h, in which the organic parts were partially removed and the remaining ones were transformed to amorphous carbon. On the other hand, the inorganic parts formed WO_3 through condensation. Thus, the resulting composite film became a mesoporous amorphous carbon/WO_3 structure. Finally, the amorphous carbon/WO_3 was exposed to O_2 plasma to eliminate amorphous carbon. The Raman spectrum of amorphous carbon/WO_3 (Fig. S1a) shows two broad peaks at approximately 1375 and 1595 cm^{-1} corresponding to the D and G peaks arising from amorphous carbons[55,56]. After the O_2 plasma treatment, the amorphous carbons are fully removed, which is confirmed through the disappearance of the D and G peaks shown in Fig. S1b. It is noted that the O_2 plasma treatment is an effective method to selectively remove the amorphous carbon without promoting further WO_3 crystalline growth because the activation energy of the grain growth of WO_3 is higher than that of the plasma[57]. However, when the thermal treatment (e.g., 400 °C) is performed to remove amorphous carbons, crystalline WO_3 phases can be developed, which prevents effective ion diffusion through the WO_3 film (see the X-ray diffraction (XRD) pattern and scanning electron microscopy (SEM) image in Figs. S2a, b, respectively). The SEM image supports the mesoporous structure of the WO_3 film with small pores having an average diameter of ~30 nm (Fig. 1b). The thickness of the mesoporous structure of the WO_3 film is determined to be ~250 nm (see the cross-section SEM image in the inset of Fig. 1b).

Figure 1c shows the X-ray photoelectron spectroscopy (XPS) of the W 4f spectrum of the mesoporous WO_3 film. Two peaks at 35.5 and 37.7 eV are observed, corresponding to W $4f_{7/2}$ and W $4f_{5/2}$ of the electronic state of W^{6+} in WO_3, respectively[58,59]. It is known that a high EC performance can be obtained when amorphous WO_3 is employed because of the easier ion penetration into the film[60–63]. Therefore, we investigated the crystalline structure of the mesoporous WO_3 film using XRD, high-resolution transmission electron microscopy (HR-TEM), and selected area electron diffraction (SAED) (Fig. 1d, e). Figure 1d shows the XRD patterns of the mesoporous WO_3 film on FTO glass and bare FTO glass. Distinct diffraction peaks are not observed from the WO_3 film, implying its amorphous nature[64]. The amorphous nature of WO_3 is further supported by the HR-TEM image and SEAD pattern, in which no distinct lattice fringe is shown (Fig. 1e), but an amorphous halo in the isotropic SAED
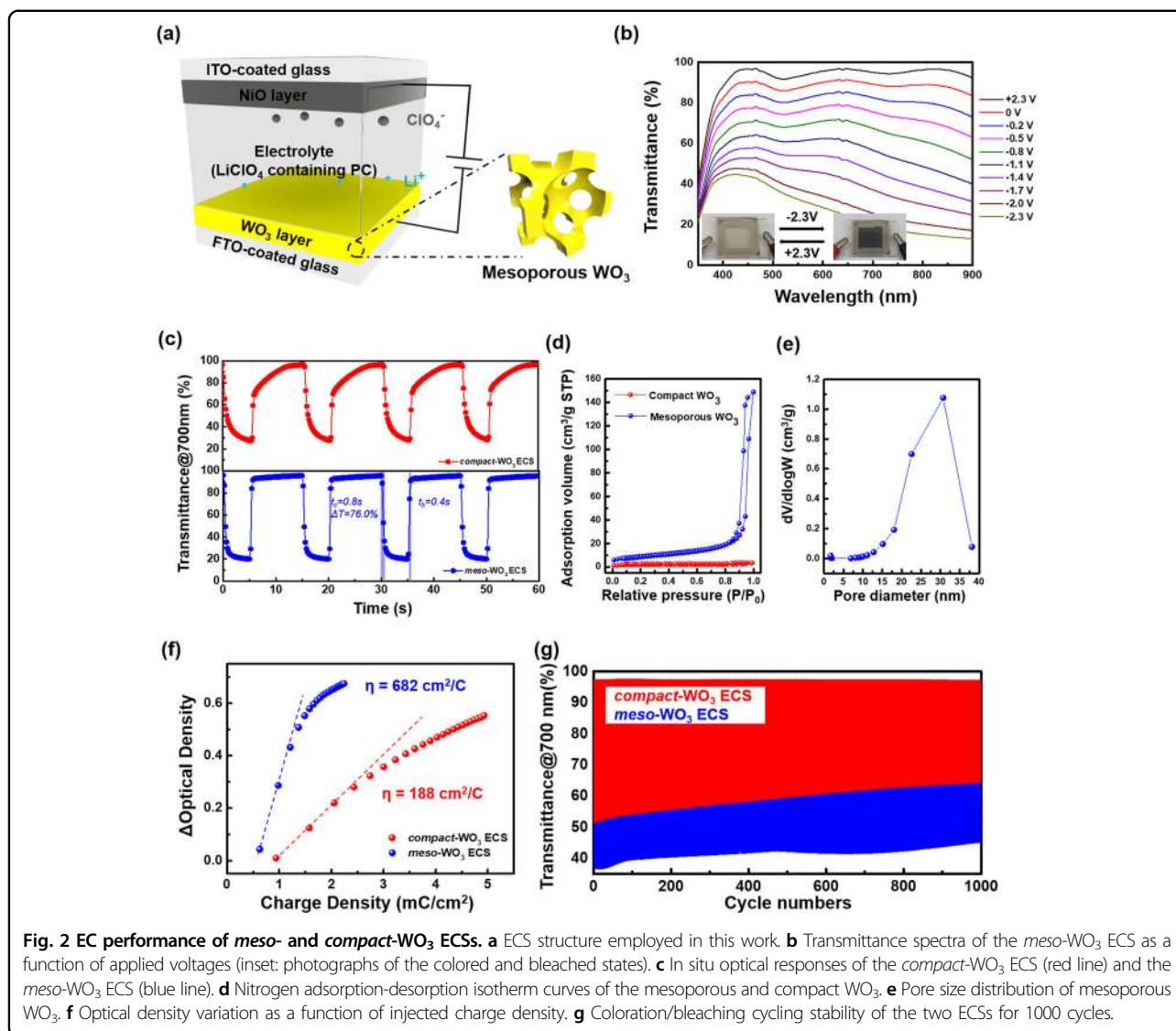
Fig. 1 Fabrication and characterization of mesoporous WO₃ films. a Schematic showing the fabrication process of the mesoporous WO₃ film. **b** SEM image (top view) of the mesoporous WO₃ film (inset: cross-sectional view). **c** W 4f XPS spectra of the mesoporous WO₃ film. **d** XRD patterns of the mesoporous WO₃ film and bare FTO glass. **e** HR-TEM image of the mesoporous WO₃ film (inset: SAED pattern).

pattern is shown (inset of Fig. 1e). Accordingly, a high electrolyte-ion accessibility to the WO₃ surface and high ion diffusivity into the WO₃ film are anticipated based on the large surface area of the mesoporous structure and the amorphous nature of WO₃, respectively. As a result, the ultrafast dynamics of mesoporous WO₃-based ECSs (denoted *meso*-WO₃ ECS) are expected.

Figure 2a depicts the schematic of the *meso*-WO₃ ECS with an electrolyte (1 M LiClO₄ in propylene carbonate (PC)) and NiO film (ion-storage layer). The characterizations of the NiO film using XRD, XPS, and SEM are shown in Fig. S3a–c, respectively. For comparison, we also fabricated devices denoted as *compact*-WO₃ ECS, in which WO₃ films were prepared by WO₃ nanoparticles (see the XRD pattern, XPS spectra, and SEM image of the compact-WO₃ film in Fig. S4a–c). The thickness of the compact-WO₃ film (~260 nm) is quite similar to that (~250 nm) of the mesoporous WO₃ film. To investigate

the electrochromic (EC) behavior of these ECSs, we recorded the UV–vis transmittance spectra of the *meso*-WO₃ ECS at various applied voltages (Fig. 2b). As the applied voltage is increased, the transmittance gradually decreases over the entire range of visible light wavelengths, which is caused by the formation of reduced WO₃ (W^{5+}) and oxidized NiO (Ni^{3+}). On the other hand, when +2.3 V is applied, the transparent bleached state is recovered by producing oxidized WO₃ (W^{6+}) and reduced NiO (Ni^{2+}). While the device is highly transparent in the bleached state, a blue-colored state is observed in the colored state (see also the inset of Fig. 2b). A similar optical transition is observed from the *compact*-WO₃ ECS (Fig. S5).

However, there is a significant difference in the dynamic responses of the device, which is one crucial metric for evaluating ECS performance. The response times of coloration (t_c)/bleaching (t_b) are defined as the time at which
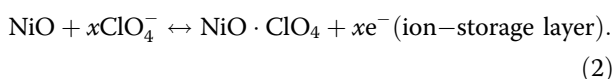
Fig. 2 EC performance of *meso-* and *compact*-WO₃ ECSs. a ECS structure employed in this work. **b** Transmittance spectra of the *meso*-WO₃ ECS as a function of applied voltages (inset: photographs of the colored and bleached states). **c** In situ optical responses of the *compact*-WO₃ ECS (red line) and the *meso*-WO₃ ECS (blue line). **d** Nitrogen adsorption-desorption isotherm curves of the mesoporous and compact WO₃. **e** Pore size distribution of mesoporous WO₃. **f** Optical density variation as a function of injected charge density. **g** Coloration/bleaching cycling stability of the two ECSs for 1000 cycles.

90% of the maximum transmittance contrast (ΔT_{max}) is achieved. To compare the EC dynamic responses of the above two devices, we recorded the transmittance profiles at 700 nm at alternating potentials (+2.3 V, 5 s and −2.3 V, 10 s) (Fig. 2c). The *meso*-WO₃ ECS exhibits large optical modulation ($\Delta T_{max} = 76\%$) and ultrafast coloration ($t_c = 0.8$ s) and bleaching time ($t_b = 0.4$ s), which is notably faster than previously reported WO₃-based ECDs (Table S1). In the case of the *compact*-WO₃ ECS, under the same operating conditions as those for *meso*-WO₃, a stable state of coloration and bleaching is not obtained and shows a lower optical modulation (69.2%), indicating a slower dynamic response. After a sufficient coloration (30 s) and bleaching times (30 s), ΔT_{max} is determined to be ~78% similar to that (~76%) of the *meso*-WO₃ ECS (Fig. S6). However, a much slower response is observed with t_c and t_b values of ~6.8 and ~9.2 s (Fig. S6),

respectively, compared to those (~0.8 and ~0.4 s) of meso-WO₃. To elucidate the origin of such different behaviors, we conducted a nitrogen adsorption-desorption experiment to investigate the larger surface area of mesoporous WO₃ (Fig. 2d). Similar to conventional mesoporous samples[44,45], mesoporous WO₃ shows a Type-IV isotherm, and the BET surface area (S_{BET}) is measured to be 32.14 m²/g. The pore size distribution derived from the adsorption branch was also investigated using the BJH method, resulting in an average diameter of ~29.3 nm (Fig. 2e). On the other hand, compact WO₃ shows a much smaller surface area (S_{BET} with 6.4 m²/g).

Another factor for evaluating the performance of ECSs is the coloration efficiency (η), which is calculated from the slope of the linear regime of the optical density variation as a function of injected charge density. The coloration efficiencies of *meso*-WO₃ and *compact*-

WO_3 ECSs are calculated to be 682 and 188 cm^2/C, respectively (Fig. 2f). Accordingly, the *meso*-WO_3 ECS consumes less energy than the *compact*-WO_3 ECS. Cycling stability under fast response conditions is required for practical ECSs such as smart windows and electrochemical reflective displays. Figure 2g shows the transmittance responses of both ECSs during a 1000-cycle test. Under quick switching conditions (e.g., coloration/bleaching of 1 s/5 s), the *meso*-WO_3 ECS maintains 85.5% of the original optical modulation after 1000 cycles, whereas the drop in optical modulation of the *compact*-WO_3 ECS is 70.7% (see also the changes in $\Delta T/\Delta T_0$ of both ECSs in Fig. S7). Li$^+$ ions are repeatedly inserted and extracted in the WO_3 and NiO films during the cycling test with alternating potentials. However, Li$^+$ ions are gradually trapped in both films. As a result, unchangeable and transparent W^{6+} and Ni^{2+} are present in the forms of $Li_{2x}W_2O_{6+x}$ and $Li_{2y}Ni_2O_{2+y}$, respectively[65]. These species do not participate in the redox reactions, so the color intensity is reduced while the bleached state is not affected. The excellent cycling stability of the *meso*-WO_3 ECS even with fast switching is attributed to their mesoporous WO_3 structure with a large surface area. Therefore, we conclude that the *meso*-WO_3 ECS is more suitable for dynamic applications (e.g., displays) that require a fast response.

Considering the electrochemical reactions (Eqs. (1) and (2)) during coloration/bleaching, ECSs can store energy via ion insertion/extraction processes. Therefore, we investigated and compared the capacitive performances of the *meso*-WO_3 and *compact*-WO_3 ECSs.

$$WO_3 + xLi^+ + xe^- \leftrightarrow Li_xWO_3 \text{(EC layer)}, \tag{1}$$

$$NiO + xClO_4^- \leftrightarrow NiO \cdot ClO_4 + xe^- \text{(ion−storage layer)}. \tag{2}$$

Electrochemical impedance spectroscopy (EIS) characterizations were conducted to compare the charge transfer and ion kinetics of the *meso*-WO_3 and *compact*-WO_3 ECSs. From the Nyquist plots (Fig. S8), the *meso*-WO_3 ECS shows a lower intercept at the real axis and a smaller semicircle than those of the *compact*-WO_3 ECS, indicating a smaller contact resistance and charge transfer resistance. Additionally, a larger slope in the Warburg region of the *meso*-WO_3 ECS compared to that of the *compact*-WO_3 ECS represents a lower ion diffusion resistance. All the EIS fitting results are summarized in Table S2. Figure S9 shows the cyclic voltammetry (CV) curves of the *meso*-WO_3 and *compact*-WO_3 ECSs at various scan rates from 200 to 1500 mV/s. All the CV curves exhibit pseudocapacitive behaviors with redox peaks. However, particularly at high scan rates (e.g., 1500 mV/s), the *meso*-WO_3 ECS

maintains its characteristic CV curves, while the CV curves of the *compact*-WO_3 ECS are severely distorted. The fast electrochemical kinetics of *meso*-WO_3 may be attributed to its fast charge transfer and ion kinetics. Figure 3a displays the galvanostatic charging/discharging (GCD) curves of the *meso*-WO_3 ECS at various current densities (see also the GCD curves of the *compact*-WO_3 ECS in Fig. S10). For quantitative analysis, the areal capacitance (C) is calculated from discharging curves using[23,66].

$$C = \frac{I\Delta t}{S\Delta V}. \tag{3}$$

For example, the C values of the *meso*-WO_3 ECS and *compact*-WO_3 ECS are determined to be 2.57 and 2.51 mF/cm^2, respectively, at the lowest current density in this study (i.e., 0.02 mA/cm^2). However, there is a significant difference in the charge-storing capability as the operating current density increases (Fig. 3b). The capacitance of the *compact*-WO_3 ECS is greatly decreased compared with that of the *meso*-WO_3 ECS. For instance, the capacitance retentions of the *meso*-WO_3 and *compact*-WO_3 ECSs are 68 and 34%, respectively, when the current density is changed from 0.02 to 1.0 mA/cm^2. The areal capacitance values at various current densities are shown in Fig. S11. Furthermore, from the Ragone plots of both ECSs (Fig. S12), the *meso*-WO_3 ECS exhibits an energy density of 15.8 Wh/kg at a power density of 0.2 kW/kg. Even at a high power density of 9.6 kW/kg, the energy density is measured to be 10.6 Wh/kg, which is much higher than that (4.9 Wh/kg) of the *compact*-WO_3 ECS at a similar power density of 8.8 kW/kg. This result implies that the *meso*-WO_3 ECS is more promising for quick charging/discharging devices. Indeed, the long-term charging/discharging stability of the *meso*-WO_3 ECS at 1.0 mA/cm^2 is remarkably outstanding (Fig. 3c). Only a 6.2% reduction in the first run is detected after 1000 cycles, whereas the *compact*-WO_3 ECS deteriorates considerably under the same conditions. For example, only 14% of the initial areal capacitance is maintained after 1000 cycles.

Another fascinating function of ECSs was also examined, in this case, the direct visualization of the stored energy level. We simultaneously recorded the GCD curve at 1.0 mA/cm^2 and the corresponding in situ transmittance profile at 700 nm of the *meso*-WO_3 ECS (Fig. 3d). As the device is charged to −2.3 V, the transmittance decreases (i.e., colored). In contrast, during discharging, the transmittance increases and eventually returns to its initial transmittance. Photographs of the *meso*-WO_3 ECS at six representative stages during charging/discharging are shown in Fig. 3e, where the device indicates the real-time level of the stored energy
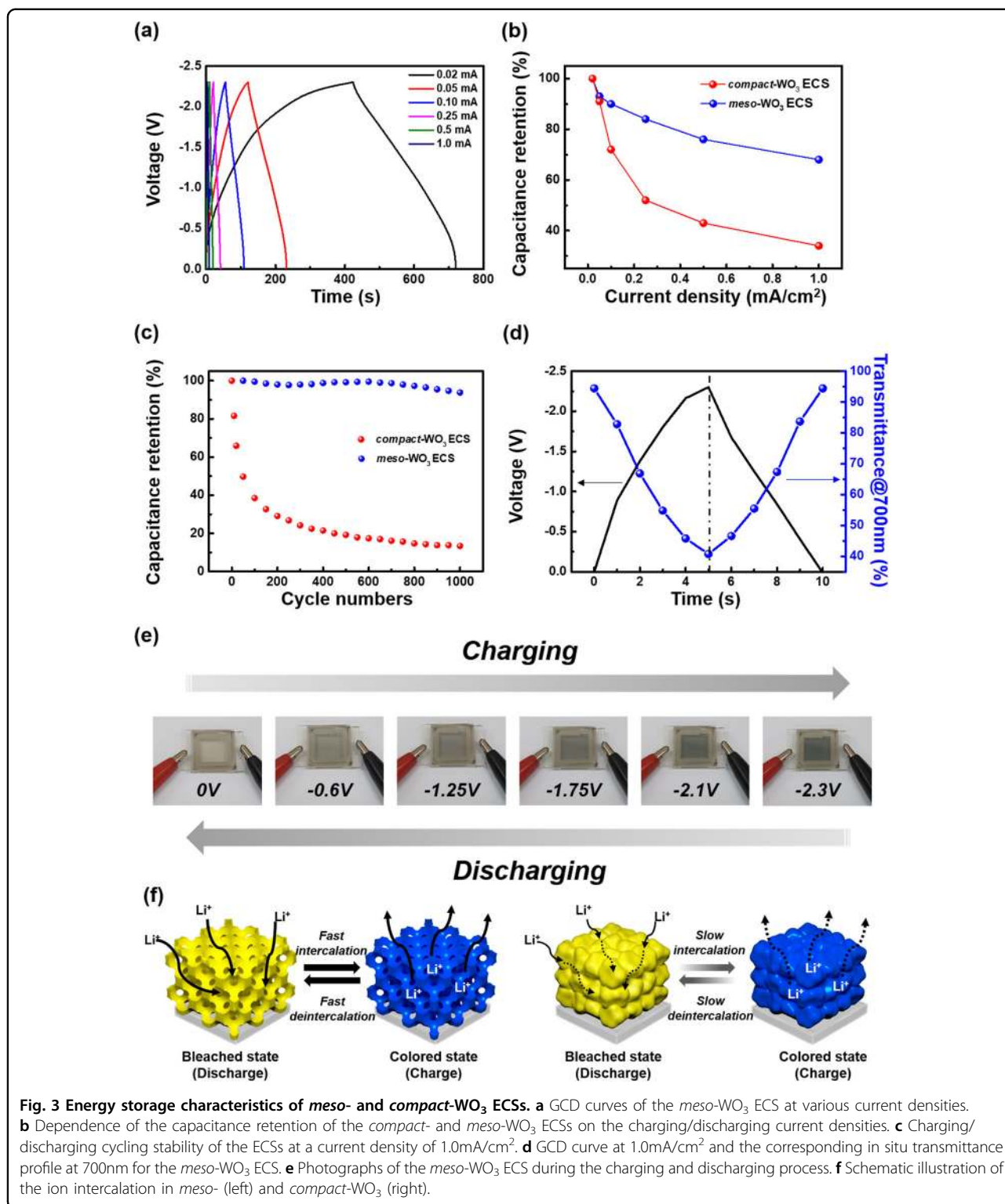
Fig. 3 Energy storage characteristics of *meso*- and *compact*-WO$_3$ ECSs. a GCD curves of the *meso*-WO$_3$ ECS at various current densities. **b** Dependence of the capacitance retention of the *compact*- and *meso*-WO$_3$ ECSs on the charging/discharging current densities. **c** Charging/discharging cycling stability of the ECSs at a current density of 1.0mA/cm^2. **d** GCD curve at 1.0mA/cm^2 and the corresponding in situ transmittance profile at 700nm for the *meso*-WO$_3$ ECS. **e** Photographs of the *meso*-WO$_3$ ECS during the charging and discharging process. **f** Schematic illustration of the ion intercalation in *meso*- (left) and *compact*-WO$_3$ (right).

through its color intensity. Regardless of the current density, the *meso*-WO$_3$ ECS exhibits a symmetrical GCD profile shape and no significant degradation of optical contrast, which is attributed to its effective and fast ion transport (Fig. S13). In the case of the *compact*-WO$_3$ ECS, the GCD profiles become more asymmetrical in shape, and the optical modulation dramatically decreases as the current density increases (Fig. S14). These results
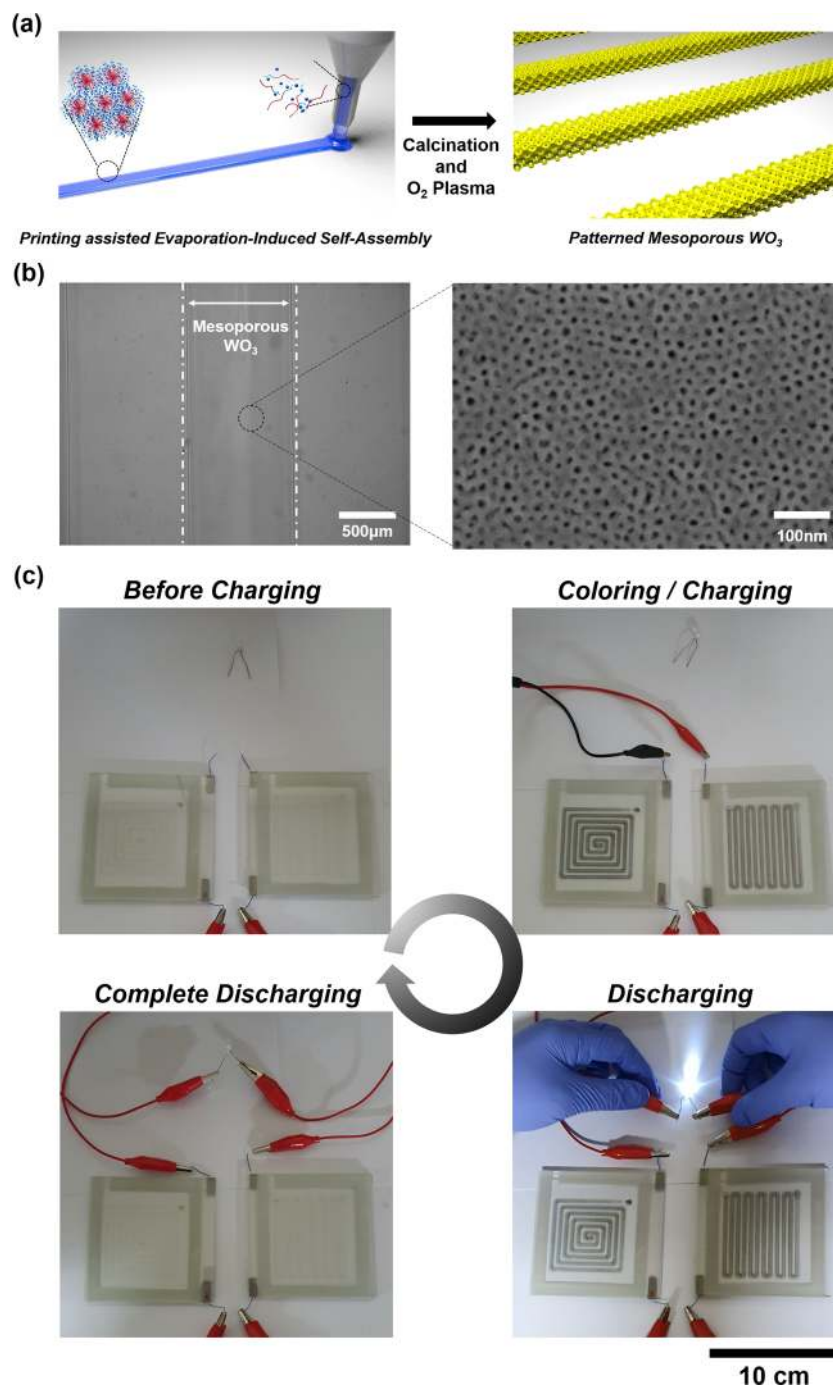
Fig. 4 Application of PEISA for the fabrication of functional ECSDs. a Schematic illustration of PEISA. **b** OM (left) and SEM (right) images of mesoporous WO₃ fabricated by PEISA. **c** Photographs of the ECSD during the reversible charging (coloration of the pattern) and discharging (LED light on and bleaching) test. For this application, two ECSDs were connected in series.

suggest that the *compact*-WO₃ ECS is not proper for high-rate operations due to its inefficient ion transport and slow charge transfer. Similar to the origin of its outstanding kinetic EC performance, the availability of the quick charging/discharging of *meso*-WO₃ ECS arises

from the large surface area of the mesoporous WO₃ and its amorphous nature, in which the fast ion diffusion and simultaneous intercalation/deintercalation of large amounts of ions can occur (Fig. 3f (left)). In contrast, the behavior of the *compact*-WO₃ ECS is related to its low

ion and charge transfer because of its very small surface area and its crystalline nature, which causes incomplete ion deintercalation (Fig. 3f (right)).

Last, we demonstrated highly functional energy-storing ECS displays (ECSDs) by combining printing and EISA protocols, referred to as printing-assisted EISA (PEISA) (Fig. 4a). When the EISA solution is printed out of the nozzle, a micellar structure is directly produced through evaporation. When a sequential calcination and O_2 plasma treatment are performed, patterned mesoporous WO_3 is prepared. Figure 4b shows the optical microscopy (OM) and SEM images of the printed mesoporous WO_3. Well-defined mesoporous WO_3 is clearly observed in the printed lines. This result implies that user-defined patterns consisting of mesoporous WO_3 can be fabricated by PEISA, which can then be applied to energy-storing ECSDs. To complete device fabrication, we also patterned NiO with the same shape as WO_3, followed by sandwiching the electrolyte layers with mesoporous WO_3. The resulting ECSD successfully functions as both an electrochemical reflective display and an energy storage device (Fig. 4c). When the device is charged, the patterns turn dark blue, indicating the charged state. To observe the utilization of the charged energy, the ECSD was connected to a white light-emitting diode (LED). Initially, the LED emits light, and then the ECSD returns to its original transparent state when the stored energy is completely consumed.

Conclusions

In this study, multifunctional ECSs were fabricated based on amorphous mesoporous WO_3 films produced by EISA. Compared to the *compact*-WO_3 ECS, the *meso*-WO_3 ECS exhibited superior EC and supercapacitor performance based on its large surface area and the amorphous WO_3. For example, the *meso*-WO_3 ECS exhibited a large optical modulation (~76%), ultrafast dynamics (t_c = 0.8 s, t_b = 0.4 s), and high areal capacitance (2.57 mF/cm^2), even at a high current density. Moreover, the *meso*-WO_3 ECS exhibited excellent coloration/bleaching and charging/discharging cycling stability under rapid operating conditions (frequent switching or high current operations). Additionally, we developed PEISA to fabricate patterned mesoporous WO_3 for ultrafast ECSDs, which could serve as electrochemical reflective displays that could also store electrical charge. The stored energy was used for powering other electronic devices, while the color intensity of the pattern indicated the level of stored energy. These results show that the ECSD in this work has tremendous potential for use in next-generation smart electronics. Our ongoing work aims to improve the performance of these ECSDs through the optimization of the pore diameter and film thickness along with the doping of various other metals (e.g., Ti, Mo, Sb, etc.) into the mesoporous structure. Since the PEISA method introduced in this study can be easily

employed to prepare various mesoporous metal oxides, such as TiO_2, Al_2O_3, V_2O_5, and ZnO, this method provides a versatile foundation for producing printed electronics.

Experimental section
Materials

All chemicals were purchased from Sigma-Aldrich (St. Louis, MO, USA) except *tert*-butyl alcohol (>99.0%, Tokyo Chemical Industry Co., Ltd., Japan) and polystyrene-*block*-polyethylene oxide (PS-*b*-PEO, polydispersity index (PDI) = 1.09, M_n (PS) = 19,000 g mol^{-1}, M_n (PEO) = 6500 g mol^{-1}, Polymer Source Inc., Canada). Indium tin oxide (ITO)-coated (sheet resistance: 15 Ω/sq) and fluorine-doped tin oxide (FTO)-coated glasses (sheet resistance: 15 Ω/sq) were purchased from Asahi Glass Co (Tokyo, Japan). The ITO and FTO-coated glasses were cleaned with 2-propanol (15 min) under sonication. Then, further cleaning with a UV-ozone treatment was conducted for 15 min before use.

Fabrication of the mesoporous and compact-WO_3 films

Mesoporous WO_3 films were prepared using amphiphilic PS_{19k}-*b*-$PEO_{6.5k}$ as the structure directing agent and WCl_6 as the precursor. PS_{19k}-*b*-$PEO_{6.5k}$ (50 mg) was dissolved in THF (1 g), while WCl_6 (0.2 g) was separately dissolved in EtOH (0.4 g). The two above solutions were mixed in a weight ratio of 2 (PS_{19k}-*b*-$PEO_{6.5k}$ solution):1 (WCl_6 solution), and then the solution was kept at 45 °C. After 24 h, the obtained blue solution was spin-coated onto FTO glass at 1000 rpm for 5 s. Subsequently, the thin film-coated FTO glass was placed in an oven at 45 °C for 24 h to form an inorganic-polymer composite. Next, the inorganic-polymer composite film was calcined in a preheated 350 °C furnace for 1 h, which resulted in an amorphous carbon/WO_3 film. Last, an O_2 plasma treatment was conducted to remove amorphous carbon while maintaining the amorphous nature of WO_3. Additionally, we prepared compact-WO_3 films for comparison. Compact-WO_3 films were prepared by spin coating a nanoparticle WO_3 suspension on FTO glass at 5000 rpm for 20 s, followed by thermal annealing at 60 °C for 10 h in vacuum [23].

Fabrication of the NiO film

NiO nanoparticles were synthesized by the solvothermal method according to a previous report[67]. The resulting NiO nanoparticles (0.2 g) were dispersed in a mixture of DI-water and 2-propanol as the solvent (DI-water:2-propanol = 1:1, 2 g). Thereafter, the obtained suspension was spin coated onto ITO glass at 1000 rpm for 20 s, followed by annealing at 200 °C for 2 h.

Device assembly

ECSs were fabricated by assembling the mesoporous WO_3 (or compact-WO_3 film) and NiO film as an active layer and ion-storage layer, respectively, in which a precut

thermoplastic (Parafilm) spacer was employed. Then, 1 M $LiClO_4$ in a propylene carbonate (PC) electrolyte was filled into the assembled ECSs and sealed with epoxy glue.

Printing-assisted EISA

The EISA solution was filled into a syringe, which had a nozzle diameter of 160 μm. An electrostatic field was applied between the nozzle and the substrate during printing, and the electrostatic force allowed the polar EISA solution to form a well-defined pattern. The movement of the sample stage was controlled by a computer, by which the printing speed and the distance between the nozzle and substrate were adjusted. The obtained patterned films were calcined at 350 °C, followed by an O_2 plasma treatment before use.

Film characterization

The fabricated films in this work were characterized by OM (ECLIPSE LV100ND, Nikon), FE-SEM (S-4800, Hitachi) at an acceleration voltage of 10 kV, HR-TEM (JEM-2200FS, JEOL), XRD (D/MAX2500 VL-PC, Rigaku) with a Cu Kα radiation source ($\lambda = 0.154178$ nm), XPS (Vgescalab 250, Thermo Fisher Scientific) equipped with a monochromatic Al-Kα radiation source ($h\nu = 1486.8$ eV) and Raman spectroscopy (Alpha 300 R, WITEC) using a He–Ne laser with an excitation wavelength of 632.8 nm. Nitrogen physisorption was performed at 77 K using a Micrometrics ASAP 2010 system. The Brunauer-Emmett-Teller (BET) surface area was calculated using the data obtained over the relative pressure range of $0.05 \leq p/p_0 \leq 0.2$. The cell and window size distributions were calculated by the Barrett–Joyner–Halenda (BJH) method from the adsorption and desorption branches of the isotherm.

Performance characterizations

DC voltage and square wave voltages were supplied from a potentiostat (Wave Driver 10, Pine Instrument). A UV–vis spectrophotometer (V-730, Jasco) was used to record the UV–vis spectra (360 to 1100 nm at a scan rate of 400 nm/min) at various applied voltages and the transient transmittance changes at a fixed wavelength (700 nm). CV, EIS, and galvanostatic charge–discharge (GCD) measurements were conducted using a battery cycler system (WBCS3000L, WonATech). EIS was conducted from 1000 kHz to 0.01 Hz at −0.5 V.

Author details
[1]National Creative Research Initiative Center for Smart Block Copolymer Self-Assembly, Department of Chemical Engineering, Pohang University of Science and Technology (POSTECH), Pohang, Gyungbuk 790-784, Republic of Korea. [2]Department of Chemical Engineering, University of Seoul, Seoul 02504, Republic of Korea. [3]Department of Materials Science and Engineering, Pohang University of Science and Technology (POSTECH), Pohang, Gyungbuk 790-784, Republic of Korea. [4]Department of Advanced Materials Engineering, Yeungnam University, Gyeongsan 38541, Republic of Korea

Publisher's note
Springer Nature remains neutral with regard to jurisdictional claims in published maps and institutional affiliations.

References
1. Llordes, A., Gracia, G., Gazquez, J. & Milliron, D. J. Tunable near-infrared and visible-light transmittance in nanocrystal-in-glass composites. *Nature* **500**, 323–326 (2013).
2. Wen, R.-T., Granqvist, C. G. & Niklasson, G. A. Eliminating degradation and uncovering ion-trapping dynamics in electrochromic WO_3 thin films. *Nat. Mater.* **14**, 996–1001 (2015).
3. Liu, H.-S. et al. Highly transparent to truly black electrochromic devices based on an ambipolar system of polyamides and viologen. *NPG Asia Maer.* **9**, e388 (2017).
4. Granqvist, C. G. Electrochromics for smart windows: oxide-based thin films and devices. *Thin Solid Films* **564**, 1–38 (2014).
5. Kim, K.-W. et al. Electrostatic-force-assisted dispensing printing of electrochromic gels for low-voltage displays. *ACS Appl. Mater. Interfaces* **9**, 18994–19000 (2017).
6. Wang, K., Wu, H., Meng, Y., Zhang, Y. & Wei, Z. Integrated energy storage and electrochromic function in one flexible device: an energy storage smart window. *Energy Environ. Sci.* **5**, 8384–8389 (2012).
7. Yuksel, R. et al. A novel blue to transparent polymer for electrochromic supercapacitor electrodes. *Electroanalysis* **30**, 266–273 (2018).
8. Zhou, F. et al. Perovskite photovoltachromic supercapacitor with all-transparent electrodes. *ACS Nano* **10**, 5900–5908 (2016).
9. Xia, X. et al. Controllable growth of conducting polymers shell for constructing high-quality organic/inorganic core/shell nanostructures and their optical-electrochemical properties. *Nano Lett.* **13**, 4562–4568 (2013).
10. Zhong, Y. et al. Electrochromic asymmetric supercapacitor windows enable direct determination of energy status by the naked eye. *ACS Appl. Mater. Interfaces* **9**, 34085–34092 (2017).
11. Ginting, R. T., Ovhal, M. M. & Kang, J.-W. A novel design of hybrid transparent electrodes for high performance and ultra-flexible bifunctional electrochromic-supercapacitors. *Nano Energy* **53**, 650–657 (2018).
12. Wei, D. et al. A nanostructured electrochromic supercapacitor. *Nano Lett.* **12**, 1857–1862 (2012).
13. Tian, Y. et al. Synergy of W18O49 and polyaniline for smart supercapacitor electrode integrated with energy level indicating functionality. *Nano Lett.* **14**, 2150–2156 (2014).
14. Wei, H., Zhu, J., Wu, S., Wei, S. & Guo, Z. Electrochromic polyaniline/graphite oxide nanocomposites with endured electrochemical energy storage. *Polymer* **54**, 1820–1831 (2013).
15. Mandal, D., Routh, P. & Nandi, A. K. A new facile synthesis of tungsten oxide from tungsten disulfide: structure dependent supercapacitor and negative differential resistance properties. *Small* **14**, 1702881 (2018).

16. Zheng, H. et al. Nanostructured tungsten oxide—properties, synthesis, and applications. *Adv. Funct. Mater.* **21**, 2175–2196 (2011).

17. Cong, S., Tian, Y., Li, Q., Zhao, Z. & Geng, F. Single-crystalline tungsten oxide quantum dots for fast pseudocapacitor and electrochromic applications. *Adv. Mater.* **26**, 4260–4267 (2014).

18. Xu, J. et al. High-energy lithium-ion hybrid supercapacitors composed of hierarchical urchin-like WO$_3$/C anodes and MOF-derived polyhedral hollow carbon cathodes. *Nanoscale* **8**, 16761–16768 (2016).

19. Koo, B.-R., Jo, M.-H., Kim, K.-H. & Ahn, H.-J. Multifunctional electrochromic energy storage devices by chemical cross-linking: impact of a WO$_3$•2H$_2$O nanoparticle-embedded chitosan thin film on amorphous WO3 films. *NPG Asia Mater.* **12**, 10 (2020).

20. Ma, D., Wang, H., Zhang, Q. & Li, Y. Self-weaving WO$_3$ nanoflake films with greatly enhanced electrochromic performance. *J. Mater. Chem.* **22**, 16633–16639 (2012).

21. Ma, D., Shi, G., Wang, H., Zhang, Q. & Li, Y. Morphology-tailored synthesis of vertically aligned 1D WO$_3$ nano-structure films for highly enhanced electrochromic performance. *J. Mater. Chem. A* **1**, 684–691 (2013).

22. Koo, B.-R. & Ahn, H.-J. Fast-switching electrochromic properties of mesoporous WO$_3$ films with oxygen vacancy defects. *Nanoscale* **9**, 17788–17793 (2017).

23. Yun, T. Y., Li, X., Kim, S. H. & Moon, H. C. Dual-function electrochromic supercapacitors displaying real-time capacity in color. *ACS Appl. Mater. Interfaces* **10**, 43993–43999 (2018).

24. Liu, Z. et al. Three-dimensional ordered porous electrode materials for electrochemical energy storage. *NPG Asia Mater.* **11**, 12 (2019).

25. Xie, Z. et al. Integrated smart electrochromic windows for energy saving and storage applications. *Chem. Commun.* **50**, 608–610 (2014).

26. Shen, L. et al. Flexible electrochromic supercapacitor hybrid electrodes based on tungsten oxide films and silver nanowires. *Chem. Commun.* **52**, 6296–6299 (2016).

27. Yang, P. et al. Large-scale fabrication of pseudocapacitive glass windows that combine electrochromism and energy storage. *Angew. Chem. Int. Ed.* **53**, 11935–11939 (2014).

28. Cai, G. et al. Highly stable transparent conductive silver Grid/PEDOT:PSS electrodes for integrated bifunctional flexible electrochromic supercapacitors. *Adv. Energy Mater.* **6**, 1501882 (2016).

29. Zhang, J. et al. Enhanced electrochromic performance of macroporous WO$_3$ films formed by anodic oxidation of DC-sputtered tungsten layers. *Electrochim. Acta* **55**, 6953–6958 (2010).

30. Azam, A. et al. Two-dimensional WO3 nanosheets chemically converted from layered WS$_2$ for high-performance electrochromic devices. *Nano Lett.* **18**, 5646–5651 (2018).

31. Cai, G. et al. InkJet- printed all solid-state electrochromic devices based on NiO/WO$_3$ nanoparticle complementary electrodes. *Nanoscale* **8**, 348–357 (2016).

32. Liang, L. et al. High-performance flexible electrochromic device based on facile semiconductor-to-metal transition realized by WO$_3$•2H$_2$O ultrathin nanosheets. *Sci. Rep.* **3**, 1936 (2013).

33. Scherer, M. R. J., Li, L., Cunha, R. M. S., Scherman, O. A. & Steiner, U. Enhanced electrochromism in gyroid-structured vanadium pentoxide. *Adv. Mater.* **24**, 1217–1221 (2012).

34. Wei, D., Scherer, M. R. J., Astley, M. & Steiner, U. Visualization of energy: light does indicator based on electrochromic gyroid nano-materials. *Nanotechnology* **26**, 225501 (2015).

35. Yang, H. F. & Zhao, D. Y. Synthesis of replica mesostructures by the nanocasting strategy. *J. Mater. Chem.* **15**, 1217–1231 (2005).

36. Lee, J., Yoon, S., Hyeon, T., Oh, S. M. & Kim, K. B. Synthesis of a new mesoporous carbon and its application to electrochemical double-layer capacitors. *Chem. Commun.* 2177–2178 (1999).

37. Tiemann, M. Repeated templating.*Chem. Mat.* **20**, 961–971 (2008).

38. Ryoo, R., Joo, S. H. & Jun, S. Synthesis of highly ordered carbon molecular sieves via template-mediated structural transformation. *J. Phys. Chem. B* **103**, 7743–7746 (1999).

39. Jun, S. et al. Synthesis of new, nanoporous carbon with hexagonally ordered mesostructure. *J. Am. Chem. Soc.* **122**, 10712–10713 (2000).

40. Shi, Y. F., Wan, Y. & Zhao, D. Y. Ordered mesoporous non-oxide materials. *Chem. Soc. Rev.* **40**, 3854–3878 (2011).

41. Ren, Y., Ma, Z. & Bruce, P. G. Ordered mesoporous metal oxides: synthesis and applications. *Chem. Soc. Rev.* **41**, 4909–4927 (2012).

42. Brinker, C. J., Lu, Y., Sellinger, A. & Fan, H. Evaporation-Induced self-assembly: nanostructures made easy. *Adv. Mater.* **11**, 7 (1999).

43. Kang, E. et al. Block copolymer directed one-pot simple synthesis of L10-phase FePt nanoparticles inside ordered mesoporous aluminosilicate/carbon composites. *ACS Nano* **5**, 1018–1025 (2011).

44. Zhang, J. et al. Ligand-assisted assembly approach to synthesize large-pore ordered mesoporous titania with thermally stable and crystalline framework. *Adv. Energy Mater.* **1**, 241–248 (2011).

45. Zhu, Y. et al. Mesoporous tungsten oxides with crystalline framework for highly sensitive and selective detection of foodborne pathogens. *J. Am. Chem. Soc.* **139**, 10365–10373 (2017).

46. Deng, Y. et al. Crontrolled synthesis and functionalization of ordered large-pore mesoporous carbons. *Adv. Funct. Mater.* **20**, 3658–3665 (2010).

47. Deng, Y. et al. Thick wall mesoporous carbons with a large pore structure templated from a weakly hydrophobic PEO-PMMA diblock copolymer. *J. Mater. Chem.* **18**, 91–97 (2008).

48. Sanchez, C., Boissiere, C., Grosso, D., Laberty, C. & Nicole, L. Design, synthesis, and properties of inorganic and hybrid thin films having periodically organized nanoporosity. *Chem. Mater.* **20**, 682–737 (2008).

49. Mahoney, L. & Koodali, R. T. Versatility of evaporation-induced self-assembly (EISA) method for preparation of mesoporous TiO$_2$ for energy and environmental applications. *Materials* **7**, 2697–2746 (2014).

50. Xu, J., Xia, J. & Lin, Z. Evaporation-induced self-assembly of nanoparticles from a sphere-on-flat geometry. *Angew. Chem. Int. Ed.* **46**, 1860–1863 (2007).

51. Byun, M., Bowden, N. B. & Lin, Z. Hierarchically organized structures engineered from controlled evaporative self-assembly. *Nano Lett.* **10**, 3111–3117 (2010).

52. Park, W. K. et al. Large-scale patterning by the roll-based evaporation-induced self assembly. *J. Mater. Chem.* **22**, 22844–22847 (2012).

53. Yu, K, Hurd, A. J. & Eisenberg, A. Syntheses of silica/polystyrene-block-poly (ethylene oxide) films with regular and reverse mesostructures of large characteristic length scales by solvent evaporation-induced self-assembly. *Langmuir* **17**, 7961–7965 (2001).

54. Yu, K, Smarsly, B. & Brinker, C. J. Self-assembly and characterization of mesostructured silica films with a 3D arrangement of isolated spherical mesopores. *Adv. Funct. Mater.* **13**, 47–52 (2003).

55. Biccari, F. et al. Graphene-based electron transport layers in perovskite solar cells: a step-up for an efficient carrier collection. *Adv. Energy Mater.* **7**, 1701349 (2017).

56. Yang, Y. et al. Electrochemically synthesized polypyrrole/graphene composite film for lithium batteries. *Adv. Energy Mater.* **2**, 266–272 (2012).

57. Mohapatra, P. et al. Calcination does not remove all carbon from colloidal nanocrystal assemblies. *Nat. Commun.* **8**, 2038 (2017).

58. Benoit, A., Paramasivam, I., Nah, Y.-C., Roy, R. & Schmuki, P. Decoration of TiO$_2$ nanotube layers with WO$_3$ nanocrystals for high-electrochromic activity. *Electrochem. Commun.* **11**, 728–732 (2009).

59. Cai, G. F. et al. Efficient electrochromic materials based on TiO2@WO3 core/shell nanorod arrays. *Sol. Energy Mater. Sol. Cells* **117**, 231–238 (2013).

60. Taylor, D. J., Cromin, J. P., Allard, L. F. & Birnie, D. P. Microstructure of laser-fired, sol-gel-derived tungsten oxide films. *Chem. Mater.* **8**, 1396–1401 (1996).

61. Deepa, M., Saxena, T. K., Singh, D. P., Sood, K. N. & Agnihotry, S. A. Spin coated versus dip coated electrochromic tungsten oxides films: structure, morphology, optical and electrochemical properties. *Electrochim. Acta* **51**, 1974–1989 (2006).

62. Cheng, W. et al. Photodeposited amorphous oxide films for electrochromic windows. *Chem* **4**, 821–832 (2018).

63. Fang, Y., Sun, X. & Gao, H. Influence of PEG additive and annealing temperature on structural and electrochromic properties of sol-gel derived WO3 films. *J. Sol.-Gel Sci. Technol.* **59**, 145–152 (2011).

64. Yoon, M., Mali, M. G., Kim, M.-W., Al-Deyab, S. S. & Yoon, S. S. Electrostatic spray deposition of transparent tungsten oxide thin-film photoanodes for solar water splitting. *Catal. Today* **260**, 89–94 (2016).

65. Dong, D. et al. Lithium trapping as a degradation mechanism of the electrochromic properties of all-solid-state WO$_3$//NiO devices. *J. Mater. Chem. C* **6**, 9875 (2018).

66. Li, H. et al. Solution-processed porous tungsten molybdenum oxide electrodes for energy storage smart windows. *Adv. Mater. Technol.* **2**, 1700047 (2017).

67. Cai, G. et al. Electrochromo-supercapacitor based on direct growth of NiO nanoparticles. *Nano Energy* **12**, 258–267 (2015).